ISPRS Journal of Photogrammetry and Remote Sensing 87 (2014) 93–107

Contents lists available at ScienceDirect

ISPRS Journal of Photogrammetry and Remote Sensing

journal homepage: www.elsevier.com/locate/isprsjprs

Using mobile laser scanning data for automated extraction of road markings

Haiyan Guan [a], Jonathan Li [a,b,*], Yongtao Yu [b], Cheng Wang [b], Michael Chapman [c], Bisheng Yang [d]

[a] Department of Geography and Environmental Management, University of Waterloo, Waterloo, ON N2L 3G1, Canada
[b] Key Laboratory of Underwater Acoustic Communication and Marine Information Technology (MOE), Xiamen University, Xiamen, FJ 361005, China
[c] Department of Civil Engineering, Ryerson University, Toronto, ON M5B 2K3, Canada
[d] State Key Laboratory of Information Engineering in Surveying, Mapping and Remote Sensing, Wuhan University, Wuhan, HB 430079,China

ARTICLE INFO

Article history:
Received 4 April 2013
Received in revised form 8 November 2013
Accepted 9 November 2013

Keywords:
MLS data
Curb
Road markings
Intensity
Multi-threshold segmentation
Morphological operation

ABSTRACT

A mobile laser scanning (MLS) system allows direct collection of accurate 3D point information in unprecedented detail at highway speeds and at less than traditional survey costs, which serves the fast growing demands of transportation-related road surveying including road surface geometry and road environment. As one type of road feature in traffic management systems, road markings on paved roadways have important functions in providing guidance and information to drivers and pedestrians. This paper presents a stepwise procedure to recognize road markings from MLS point clouds. To improve computational efficiency, we first propose a curb-based method for road surface extraction. This method first partitions the raw MLS data into a set of profiles according to vehicle trajectory data, and then extracts small height jumps caused by curbs in the profiles via slope and elevation-difference thresholds. Next, points belonging to the extracted road surface are interpolated into a geo-referenced intensity image using an extended inverse-distance-weighted (IDW) approach. Finally, we dynamically segment the geo-referenced intensity image into road-marking candidates with multiple thresholds that correspond to different ranges determined by point-density appropriate normality. A morphological closing operation with a linear structuring element is finally used to refine the road-marking candidates by removing noise and improving completeness. This road-marking extraction algorithm is comprehensively discussed in the analysis of parameter sensitivity and overall performance. An experimental study performed on a set of road markings with ground-truth shows that the proposed algorithm provides a promising solution to the road-marking extraction from MLS data.

1. Introduction

Increasing rates of population and urbanization have led to a growing demand for transportation services. Consequently, these services require tools that can provide up-to-date information about road maintenance, pavement conditions, utility management, street fixture upgrades, safety analyses, and traffic-noise levels. The significance of this information in planning, building, and maintaining road infrastructure has stimulated an increase in numerous specialized software for road asset inventory (McCarthy et al., 2007). Efficient and inexpensive techniques for data acquisition in the field of remote sensing have been gaining popularity in road extraction and recognition of street-scene objects.

Road markings on paved roadways, as critical features in traffic management systems, have important functions in providing guidance and information to drivers and pedestrians. For example, driver-assistance systems require reliable environmental perception to improve traffic safety by informing motorists and preventing accidents. Along with pavement condition and road topography, the visibility of road markings is a key element in accidents where the road itself is the cause. Especially, in highly populated urban environments, high accident rates are caused by the absence of clearly-presented road signals (Carnaby, 2005). In order to maintain high technical standards for perfect visibility, highway maintenance departments need a practical system that can also monitor road markings.

Many studies have developed to identify road markings from digital images and videos (Charbonnier et al., 1997; Li et al., 1997; Rebut et al., 2004; McCall and Trivedi, 2006; Li et al., 2007; Wang et al., 2009; Kheyrollahi and Breckon, 2010; Danescu and Nedevschi, 2010). When it comes to road-marking detection from either digital photographs or videos, precise geometrical

* Corresponding author at: Key Laboratory of Underwater Acoustic Communication and Marine Information Technology (MOE), Xiamen University, Xiamen, FJ 361005, China; Department of Geography and Environmental Management, University of Waterloo, Waterloo, ON N2L 3G1, Canada. Tel.: +1 519 8884567; fax: +1 519 7460658
E-mail addresses: junli@xmu.edu.cn, junli@uwaterloo.ca (J. Li).

0924-2716/$ - see front matter Crown Copyright © 2013 Published by Elsevier B.V. All rights reserved.
http://dx.doi.org/10.1016/j.isprsjprs.2013.11.005

information is limited by the following environmental factors: (1) shape and type of road markings, such as solid continuous lines, arrows, and words; (2) the road surface material, such as light pavement, dark pavement, or a combination of different pavements; (3) weather conditions, and the time of day that has the greatest impact on the visibility of the road surface, (4) complex shadowing from trees and moving vehicles (McCall and Trivedi, 2006). Although work on road-marking detection from digital photographs and videos has been pursued for years, fully automated road-marking extraction has remained a challenge.

Compared to photogrammetry, laser scanning as an active remote sensing technology captures highly accurate point clouds with high point density in a relatively short time (Haala et al., 2008; Chehata et al., 2009; Ussyshkin, 2009). Typically, MLS technology is ideally suited for corridor mapping due to its "drive-by" data acquisition pattern that fully captures the road environment, including road geometry and road markings. This technology collects accurate 3D geospatial data with unprecedented detail at highway speeds and at less than traditional survey costs. In the transportation discipline, MLS is safer than other means of data collection and does not require road closures and traffic disruption, thereby reducing the overall risk of the project. More recently, a number of MLS systems have been appearing in the market due to the advancement of laser scanning-related component technologies (e.g. scanning, imaging, and positioning devices) (Graham, 2010). Although there are numerous companies and research groups offering their data-processing services and solutions concerned with road asset inventory, management, and maintenance (Gordon, 2010), MLS software and automated algorithms for extracting road features are still relatively slow compared to the advancement of MLS hardware (Yang et al., 2013).

Road markings are highly retro-reflective surfaces painted on roads; reflectance of the target in the form of intensity can be used to identify road markings (Chen et al., 2009). Based on intensity differences between road surfaces and pavement markings, Toth et al. (2008) extracted road markings as the ground control for quality assessment (QA) or quality control (QC) of the image data. Smadja et al. (2010) applied a simple threshold to intensity data for extracting road markings. Yang et al. (2012) outlined solid-edge-line and broken-lane-line markings by first applying an interpolation method to MLS points, then segmenting the geo-referenced feature image using intensity and elevation-difference information. Finally, road markings were estimated by integrating their semantic knowledge (e.g., shape, size). However, as most of these algorithms have applied a global threshold-based segmentation to the intensity data of MLS point clouds, more noise is introduced, making this method less effective in extracting road-markings. Intensity data highly depend on ranges from the scanner to objects, the incidence angles of laser pulses, and the material properties of road surfaces. Thus, intensity data need to be normalized prior to segmentation. Jaakkola et al. (2008) modeled road markings from the intensity data acquired from an FGI Roamer MLS system. The method was composed of (1) radiometric correction and segmentation of the intensity data, (2) performing morphological operations to obtain a set of segments, and (3) classifying those segments as crosswalks and other lines regarding their properties. However, the algorithm can only be used with parking space lines and zebra crossings. The radiometric calibration fitted a second-order curve that was performed between the peaks on both sides of the scanning centre. Chen et al. (2009) located road-marking candidates using adaptive thresholding, where thresholds were invariant to absolute values of laser beam returns, and extracted road markings with Hough transform clustering, followed by a refinement step with trajectory constraint and geometry check. The use of the Hough transformation for road-marking extraction is weakened by specifying the number of road markings to be detected, which is a limiting factor for complex types of road markings such as hatching and words. Vosselman (2009) introduced distance-dependent intensity normalization and connected component analysis for identifying road markings. Although several types of road markings are identified, a close view of a bicycle marking shows that the extracted markings are incomplete with distinguishable noise. The pre-defined shapes used for fitting to the road-marking segments are considered to be the cause.

Aside from road markings, other high-reflective urban elements (e.g. traffic signs, retro-reflectors, tree, and grass) and their distortion effects (e.g. saturation and blooming) may have a negative effect on road-marking extraction. Some measures, such as height information and shape criteria, need to be taken into consideration to refine the extracted road markings (Yang et al., 2012). As road markings are painted on the road surfaces, we propose a scheme that first identifies road surfaces from MLS data and then extracts road markings from the identified road data. With this scheme, the extraction of road markings is limited on road areas without interruption from other intensity-distortion causing objects.

The objective of this paper is to develop a recognition framework for road markings used in a mobile mapping system, and to analyze its performance on a variety of road-marking types selected from RIEGL VMX-450 MLS data. Section 2 describes study areas and data acquired from the RIEGL VMX-450 MLS system. Our method, presented in Section 3, aims to extract road markings. The method starts with a curb-based road extraction that separates road from non-road points by detecting height jumps caused by curbs on a set of profiles based on the vehicle trajectory data. These profiles provide an effective strategy for extracting road surfaces from a large volume of MLS data. After that, the classified road points are interpolated into a geo-referenced intensity image. Next, to reduce noise, a point-density-dependent multi-threshold segmentation method is applied to the geo-referenced intensity image for identifying road markings using a morphological operation. The conducted tests are described and analyzed in Section 4. Conclusions are presented in Section 5.

2. Test MLS data

The survey area is within Xiamen Island (longitude 118°04′04″E, latitude 24°26′46″N), a part of the City of Xiamen, which is a major city on the southeast coast of China. The data were acquired on 23 April 2012 by a RIEGL VMX-450 MLS system, which was smoothly integrated with two RIEGL VQ-450 scanners with laser pulse repetition rates (PRR) up to 550 kHz, an IMU/GNSS unit, a wheel-mounted Distance Measurement Indictor (DMI), and four high-resolution cameras. This integrated set of the VMX-450 MLS system was mounted on the roof of a vehicle travelling at an average speed of 50 km/h. The two RIEGL VQ-450 laser scanners were symmetrically configured on the left and right sides, pointing toward the rear of the vehicle at a heading angle of approximately 145°. Such a configuration is called the "Butterfly" or "X" configuration pattern. The full specification of RIEGL VQ-450 can be found at the RIEGL website (RIEGL, 2013). Note that the field of view of RIEGL VQ-450 is 360°, also termed as a "full circle" owing to the motorized mirror scanning mechanism. Thus, the scanned data of two scanners form a slant grid-like pattern.

The specification of the RIEGL VMX-450 MLS claims that the system can achieve a maximum effective measurement rate of 1.1 million point's per second and a scan speed of 400 lines per second. In this paper, point density stands for the number of MLS points/m^2 and sharply drops perpendicular to the line of travel. For example, with a speed of 50 km/h, close to the scanning center, the point density is as high as 4000–7000 points/m^2, and is about 1600 points/m^2 on the pavement 20 m away from the scanning

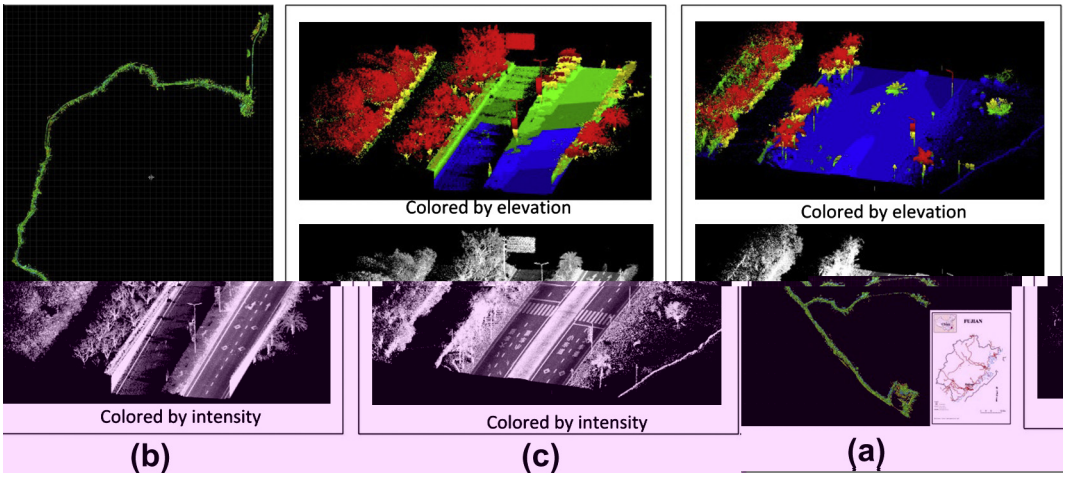

Fig. 1. Study areas and MLS data: (a) Survey route in Xiamen, China, (b) Huandao dataset and (c) ICEC dataset.

center. Roughly, the average point density on the road is about 3300 points/m^2. We sectioned two datasets from the whole survey. The first Huandao dataset has 8.4 million points in the road length of 105 m. The second ICEC dataset contains 5.4 million points covering the road length of 63 m, as shown in Fig. 1.

3. Method

To provide useful information for traffic management systems, our road-marking extraction method attempts to identify road markings from MLS point clouds. The road-marking extraction method can be seen as a stepwise procedure of interpreting MLS data. The method mainly includes the following three steps:

(1) Curb-based road extraction: the raw MLS data are partitioned, based on the vehicle trajectory data, into blocks and their corresponding profiles, by which pseudo scan-lines are formed to detect small height jumps caused by road curbs.
(2) Geo-referenced intensity image generation: the segmented road points are interpolated into a geo-referenced intensity image via an extended IDW method that combines local-and-global intensity data.
(3) Road-marking extraction: the geo-referenced intensity image is segmented by a point-density-dependent multi-threshold segmentation method to recognize road markings refined by morphological closing operations.

The rest of this section describes our method step by step. Section 3.1 elaborates on the extraction of road surfaces. Section 3.2 details the generation of geo-referenced intensity images. Section 3.3 gives road-marking extraction operations.

3.1. Curb-based road extraction

Curbs function to separate road surfaces from roadsides in an urban environment. Curb height generally ranges from 10 cm to 20 cm, depending upon a specific country's street design and construction manuals. Based on the assumption that curbs are boundaries of road surfaces, we present a curb-based method for extracting road surfaces.

We use the vehicle precise trajectory data to section the raw MLS data into a set of blocks $Block_i(i = 0, 1, \ldots N)$ at an interval (R_g), as shown in Fig. 2(a). The RIEGL MLS system, when collecting laser scanning data, records the vehicle trajectory data along the direction in which the vehicle is moving. Within each $Block_i$, a corresponding profile $profile_i$ is transversely sectioned with a certain width (S_g), as shown in Fig. 2(a). Fig. 2(b) shows a sample of the raw MLS data. The blue lines represent profiling locations. For the RIEGL MLS system used in this study, the vehicle frame is defined as the right-handed orthogonal coordinate system with its origin at an arbitrary, user-defined point. The orientation of the vehicle frame is fixed so that the x-axis is towards the front of the vehicle, the y-axis is towards the right of the vehicle and the z-axis is towards the bottom of the vehicle.

These profile images demonstrate that the curbs, vertical or nearly vertical to the road surface, are sharp height jumps; therefore, we attempt to estimate curb corners via slope and elevation-difference thresholds to separate road from non-road points. To this end, each profile is first gridded to form a pseudo scan-line with a grid width of S_p that mainly depends on point density of MLS data. Second, a sampling is implemented for each grid cell to select a principal point, as shown in Fig. 3(a). To determine the principal point within a grid cell, we use a Quick Sort algorithm to sort all the points within the grid cell according to their elevations. Starting from the lowest point, we calculate the elevation differences $\Delta L_j (j = 1, 2, 3, ..., N)$ between two consecutive points and group them into different layers. N is the number of the points in a grid cell. The two consecutive points are labelled into the same layer if and only if the elevation difference lies below a pre-defined threshold, that is, $\Delta L_j < L_T$. Otherwise, a new layer is created to separate the two points. Usually we keep $L_T = 5$ cm. Assume that points belonging to a road surface are within the lowest layer, principal points within each grid are determined by selecting the point with the highest elevation in the lowest layer. Using this scheme, most outliers such as tree points covering the road surface can be removed. The red[1] circles shown in Fig. 3(a) represent the principal points selected from grid cells. These extracted points are then re-organized into a pseudo scan-line which maintains road points and critical road features with fewer disruptive noises, as shown in Fig. 3(b).

In this study, our detection algorithm for curb corners is based on both slope and elevation-difference evaluation and implemented at the scanning center in two opposing ways. We mathematically define the slope between two consecutive points in a generated pseudo scan-line and the elevation difference of a point relative to its neighborhood in the scan-line. We use these two cri-

[1] For interpretation of color in Figs. 3 and 4, the reader is referred to the web version of this article.

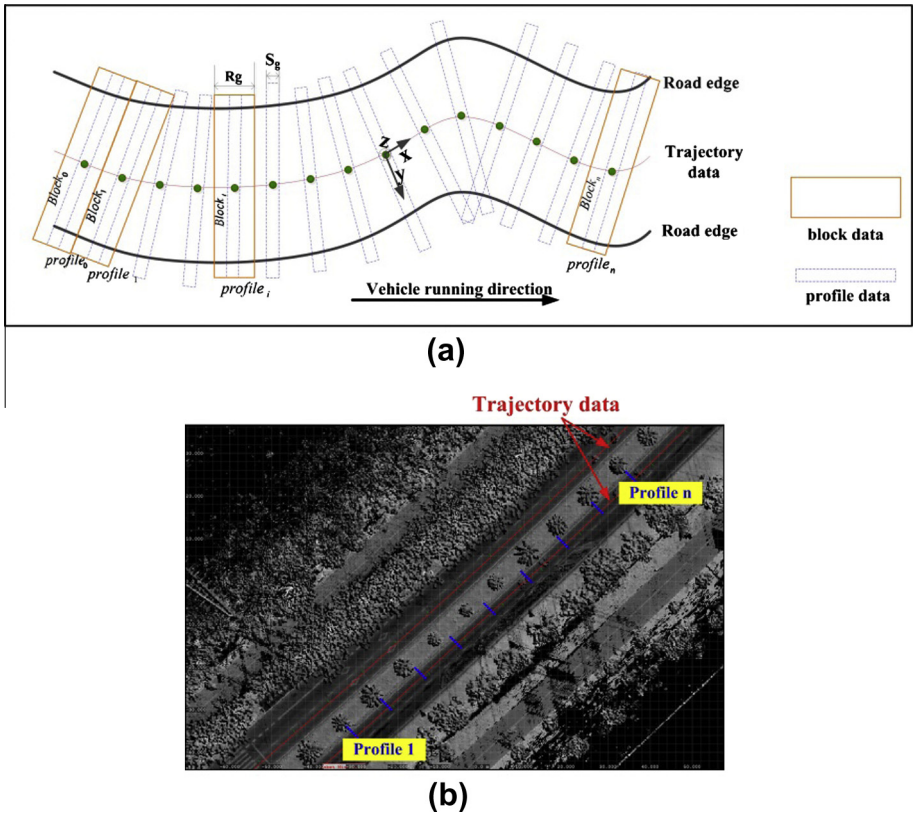

Fig. 2. An illustration of sectioning MLS data: (a) profiling illustration and (b) a sample of MLS data and its trajectory data.

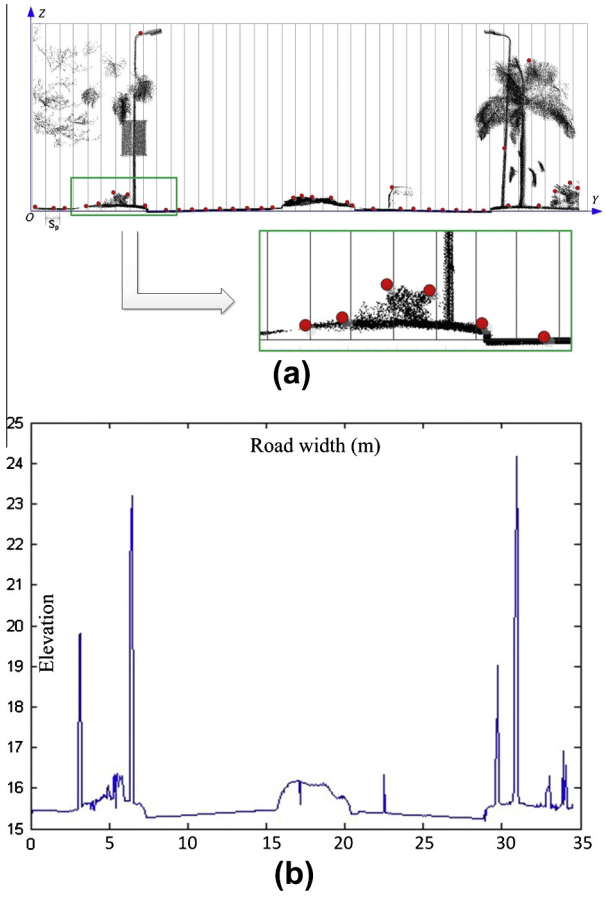

Fig. 3. A sample of a profile of MLS data: (a) a profile gridding for find the principal points and (b) a pseudo scan line.

teria to detect whether or not a point is a curb corner. First, slopes at the border of pavement and roadway are usually larger than those of continuous points on the roadway. Second, pavement points have larger elevations than road points in the neighborhood. The slope criterion detects non-road points such as cars and curbs. Then the elevation-difference criterion detects the curbs from the non-road points. Street design and construction manuals in many countries state that curb height ranges between 10 cm and 25 cm. We thus mathematically define these two observations as:

$$\forall p_i : \begin{cases} \textit{if } (S_{slope} > S_T \;\&\; (G_{\min} \leqslant G_i \leqslant G_{\max}) & \textit{curb candidate} \\ \textit{otherwise}, & \textit{non-curb} \text{ point} \end{cases} \quad (1)$$

where S_{slope} denotes the slope of two consecutive points. S_T is a given slope threshold. G_i denotes the elevation-difference of a point and its neighbor. $G_{\min}$ and $G_{\max}$ are the minimum and maximum thresholds. This definition can be described as follows: for any point p_i in the pseudo scan-line, if the slope S_{slope} is larger than S_T, as well as elevation-difference G_i at its vicinity is within the range of $[G_{\min}, G_{\max}]$, the point p_i is labeled as a curb candidate; otherwise, p_i will be labeled as a non-curb point. As the survey vehicle moves along the road, with a priori knowledge of the road, we select curb candidates closest to the scanning center as curb corners. After identifying all curb corners from the profiles, we employ a B-Spline fitting algorithm to generate two smooth road edges, and finally separate road from non-road points.

3.2. Generation of geo-referenced Intensity Images

After extracting road points from the MLS data, we rasterize the road points of interest into a geo-referenced intensity image, in which the grey value of a pixel is interpolated from its nearest neighbours using IDW interpolation. Although interpolation may cause a loss in accuracy, it is computationally efficient for processing a substantially large volume of MLS data using established

image processing algorithms. We extend the IDW interpolation stated in Yang et al. (2012) to generate a geo-referenced intensity image. The image resolution (r_g) is determined by point density, similar to the grid width (S_p) in Section 3.1.

As a variant of Yang et al. (2012), there are two rules for generating a geo-referenced intensity image:

Rule 1: a point with higher reflectivity has a greater weight;
Rule 2: a point farther away from the central point has a smaller weight.

According to the two rules, the grey value of a grid cell is calculated by:

$$G_{ij}^{I}=\left(\sum_{k=1}^{n_{ij}}W_{k}^{ij}I_{k}^{ij}\right)\Big/\left(\sum_{k=1}^{n_{ij}}W_{k}^{ij}\right)\begin{cases}W_{k}^{ij}=\alpha W_{k,ij}^{D}+\beta W_{k,ij}^{I}\\ \alpha+\beta=1.0\end{cases}, \tag{2}$$

where W_k^{ij} is the weight of the k-th point within the grid cell (i,j), I_k^{ij} is the reflectivity of the k-th point, and n_{ij} is the total number of data points within the grid cell (i,j). α and β are the weight coefficients, $W_{k,ij}^{I}$ and $W_{k,ij}^{D}$ are the weights representing Rules 1 and 2, respectively. The two weights are calculated by the following Eqs. (3) and (4):

$$W_{k,ij}^{D}=\frac{1}{r_g^2}\left(\frac{2+r_g^2}{1+D_{k,ij}^2}-2\right), \tag{3}$$

where $D_{k,ij}^2=(x_{p_{k,ij}}-x_{p_{o,ij}})^2+(y_{p_{k,ij}}-y_{p_{o,ij}})^2$, $(x_{p_{k,ij}}, y_{p_{k,ij}})$ are the coordinates of the k-th point within the grid cell (i,j), $(x_{p_{o,ij}}, y_{p_{o,ij}})$ are the coordinates of the central point within the grid cell (i,j), $D_{k,ij}$ is the distance between points $(x_{p_{k,ij}}, y_{p_{k,ij}})$ and $(x_{p_{o,ij}}, y_{p_{o,ij}})$. Eq. (3) defines the range of the weight $W_{k,ij}^{D}$ within [0,1]. The weight $W_{k,ij}^{D}=1$ when $D_{k,ij}=0$, that is, point $(x_{p_{k,ij}}, y_{p_{k,ij}})$ is at the central point $(x_{p_{o,ij}}, y_{p_{o,ij}})$ of the grid cell, indicating point $(x_{p_{k,ij}}, y_{p_{k,ij}})$ has the greatest contribution to the weight $W_{k,ij}^{D}$. On the contrary, the weight $W_{k,ij}^{D}=0$ when $Dk,ij=r_g/\sqrt{2}$ (a half of the diagonal of the grid cell), that is, point $(x_{p_{k,ij}}, y_{p_{k,ij}})$ is far most from point $(x_{p_{o,ij}}, y_{p_{o,ij}})$, indicating point $(x_{p_{k,ij}}, y_{p_{k,ij}})$ barely contributes to the weight $W_{k,ij}^{D}$.

$$W_{k,ij}^{I}=W_{k,ij}^{I1}\cdot W_{k,ij}^{I2} \tag{4}$$

$$\begin{cases}W_{k,ij}^{I1}=\frac{1}{\left(g_{\max}^{ij}-g_{\min}^{ij}\right)^2}\left(\frac{1+\left(g_{\max}^{ij}-g_{\min}^{ij}\right)^2}{1+\left(L_{k,ij}^{L}\right)^2}-1\right)\\ W_{k,ij}^{I2}=\frac{1}{\left(I_{\max}-I_{\min}\right)^2}\left(\frac{1+\left(I_{\max}-I_{\min}\right)^2}{1+\left(L_{k,ij}^{G}\right)^2}-1\right)\\ I_{k,ij}^{L}=I_{p_k,ij}-g_{\min}^{ij}\\ I_{k,ij}^{G}=I_{p_k,ij}-I_{\min}\end{cases},$$

where I_k^{ij} is the intensity value of the k-th point, $W_{k,ij}^{I1}$ and $W_{k,ij}^{I2}$ are the weights for the local and global information, $g_{\max}^{ij}$ and $g_{\min}^{ij}$ are the local maximal and minimal intensities within the grid (i,j), $I_{\max}$

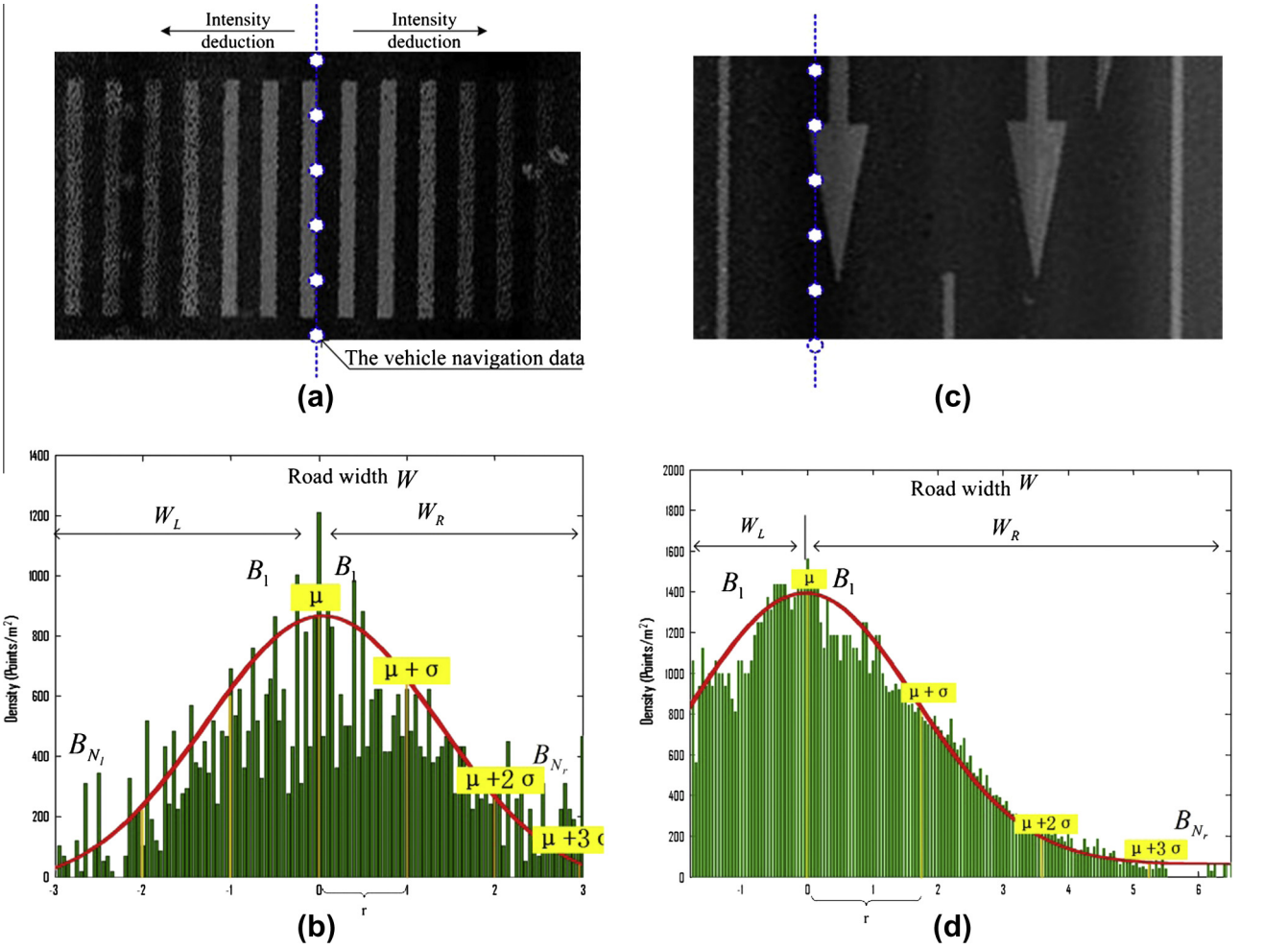

Fig. 4. Point-density-dependent multi-threshold segmentation: (a) the first road data sample, (b) statistical analysis of point density determines the number of bins to be sliced for the first data sample, (c) second road data sample and (d) statistical analysis of point density determines the number of bins to be sliced for the second data sample.

and $I_{\min}$ are the global maximal and minimal intensities of the entire road points, and $I^L_{k,ij}$ and $I^G_{k,ij}$ are the local and global intensity differences, respectively. Unlike the distance weight $W^D_{k,ij}$, the intensity weight $W^I_{k,ij}$ is divided into the following two parts: a local weight $W^{I1}_{k,ij}$ and a global weight $W^{I2}_{k,ij}$ in order to equalize the calculated pixel values of the geo-referenced intensity image. Similar to histogram equalization, a method in image processing for contrast adjustment using the image's histogram, we aim to increase the global contrast of the geo-referenced intensity image by combining the local weight $W^{I1}_{k,ij}$ with the global weight $W^{I2}_{k,ij}$. Through this adjustment, intensities can be consistently distributed on the histogram.

3.3. Road-marking extraction

On the generated geo-referenced intensity image, a threshold-based segmentation is normally carried out to obtain road markings. However, although the proposed equalization strategy lessens the intensity imbalance caused by point-density differences, the intensity values of road markings are less consistent as they gradually fades from the scanning center to its two sides, as shown in Fig. 4(a). This variation is due to the reflected intensity values that depend on (1) the scanning range from the laser sensor to the target, (2) the incidence angle of the laser beam, and (3) material properties of the target. Spontaneously, we propose a point-density-dependent multi-threshold segmentation method considering variations of scanning distance. Within different ranges of the scanning distances, local optimal segmentation thresholds are adaptively estimated.

Due to the variation of the vehicle trajectory data, the MLS data are processed block by block. As mentioned in Section 3.1, each block $Block_i$ has a corresponding profile $profile_i$. From $profile_i$, we statistically analyze its point density, as green bars shown in Fig. 4(b) and (d). Note that the point density approximates normality. Thus, a Gaussian normal distribution (red line) can be fitted to obtain two estimated parameters: mean μ and standard deviation σ. Inspired by the "68-95-99.7" rule of a normal distribution that says about 68% of values within one standard deviation σ away from the mean, about 95% of the values within two standard deviations, and about 99.7% within three standard deviations, we assume that intensity variation follows this rule. Thus, with the three-sigma rule, we define the corresponding range to vertically section data into a number of bins, on each of which we calculate an optimal threshold for segmentation.

First, according to the vehicle trajectory data and the estimated road width (W) from the extracted road data, we calculate the width of the right side (W_R) and the width of the left side (W_L) of the vehicle trajectory data. Next, the range (r) for one sigma of the fitted Gaussian normal distribution function is calculated by the estimated mean μ and standard deviation σ. Finally, the number of the bins is calculated as:

$$N_r = INT(W_R/r) + 1$$
$$N_l = INT(W_L/r) + 1 \quad (5)$$

As a result, we obtain N_s ($N_s = N_r + N_l$) bins. The number of bins varies with the vehicle trajectory data. For example, there would be six bins if the vehicle was driving close to the centre lane of the road (see Fig. 4(a) and (b)), and five bins if the vehicle was driving along the left lane of the road (see Fig. 4(c) and (d)). With the vehicle trajectory data, the fitted normal distribution of the point density can be used to determine how many bins can be sliced.

In each bin $B_i(i = 1, 2, \ldots, (N_r + N_l))$, we segment potential road markings by the Otsu's method, proposed by Otsu (1979), which is widely implemented as the default approach to image thresholding. The Otsu's method assumes that an image, which is to be divided, contains two classes: C_1 and C_2, which represents foreground (e.g. road markings) and background, respectively. The method then calculates their cumulative probabilities and mean levels, respectively. As a result, the Otsu's method can select an optimal threshold (t) that maximizes the between-class variance based on the discriminant analysis.

As a consequence, according to the vehicle trajectory data, we dynamically obtain multiple locally-optimal thresholds for segmentation. In spite of using multi-threshold segmentation, the extracted road markings still contain noise and are incomplete. By acknowledging the form and the structure of the road markings, we use a morphological operation to remove noise and extract complete road markings. The morphological operations rely only on the relative ordering of pixel values, rather than on their numerical values, and therefore are better suited to process binary images. The morphological operation used is closing, that is, dilation followed by erosion. We employ a dilation operation to remove noises and fill out holes in the extracted road markings. Subsequently, an erosion operation is used to shrink the image from both the inner and outer boundaries of the road markings.

The morphological techniques probe the road markings with a small shape or template called a structuring element; the structuring element is a small binary image, that is, a small matrix of pixels. The structuring element is related to the *size* (T), *origin*, and *shape*. The structuring element examples include square, cross, diamond, horizontal and vertical shaped. A common practice is to have odd dimensions of the structuring matrix and the *origin* defined as the centre of the matrix. Although there are many types of road markings such as crosswalks, characters, words, symbols, and arrows, most of them are linearly shaped. To simplify convolution, we use a horizontally linear shaped structuring element to dilate and erode the road markings. The linear structure with length l and direction θ is denoted by $K_{line\theta}(l)$. The direction θ is determined by the vehicle trajectory data, that is, the direction in which the vehicle is moving. A range of length l from 3 to 11 is used to determine $K_{line\theta}(l)$ for the road markings. In this study, we choose $l = 3$ pixels.

4. Results and discussions

To assess the performance of our road-marking extraction algorithm, we selected the following two sites from two surveys: Huandao and ICEC, respectively. Fig. 5 shows a close-up view of the Huandao and ICEC datasets. The displayed sections are typical urban areas, which represent the datasets that contain tall trees, low vegetation, poles, buildings, and some moving objects. It can be noted that the datasets have a variety of road markings, including longitudinal markings, transverse markings, object markings, and special markings. The longitudinal markings, provided for separating traffic flow in the same direction, can be broken, solid, or double solid. The transverse markings, marked across the direction of traffic, include stop line markings, pedestrian crossings, and direction arrows. The special markings, such as word messages, use characters to guide, regulate, or warn the road users.

4.1. Curb-based road extraction

Several parameters and their values used in the extraction of road surfaces are listed in Table 1. In this study, we chose $R_g = 3.0$ m in order to section the MLS data into a number of blocks. However, if a road has sharp bends, curves, or turns, we reduce $R_g = 1.0$ m in order to collect more curb corners for preserving road features. The trajectory data directly reflect all possible road curves by calculating the directions of GPS positions at two consecutive GPS times, and therefore determining the value of R_g. Since there are no sharp turns and curves on the roads, we chose $R_g = 3.0$ m

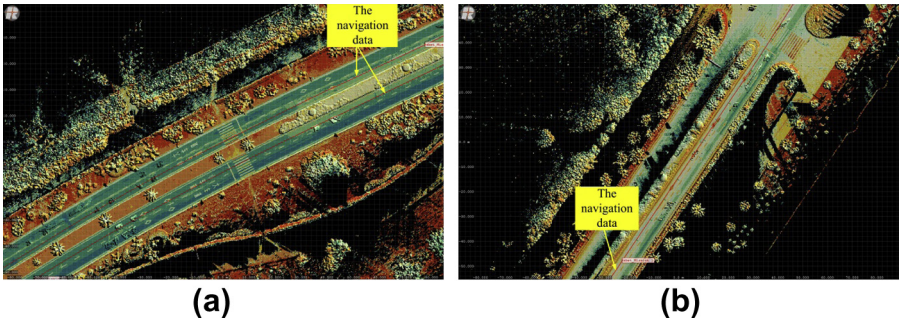

Fig. 5. A close view of a sample of raw MLS data, (a) Huangdao and (b) ICEC datasets.

Table 1
Parameters in the curb-based road surface extraction.

Name	Definition	Value
S_g	The width of a profile	~0.25 m, determined by data experiments
R_g	The length of a block data	1.0–3.0 m, automatically decided by the trajectory data
S_p	The grid size of a pseudo scan line	0.05 m, related to the point density
$G_{\min}$	The minimum height difference of the curb	0.08 m, a prior knowledge
$G_{\max}$	The maximum height difference of the curb	0.3 m, a prior knowledge

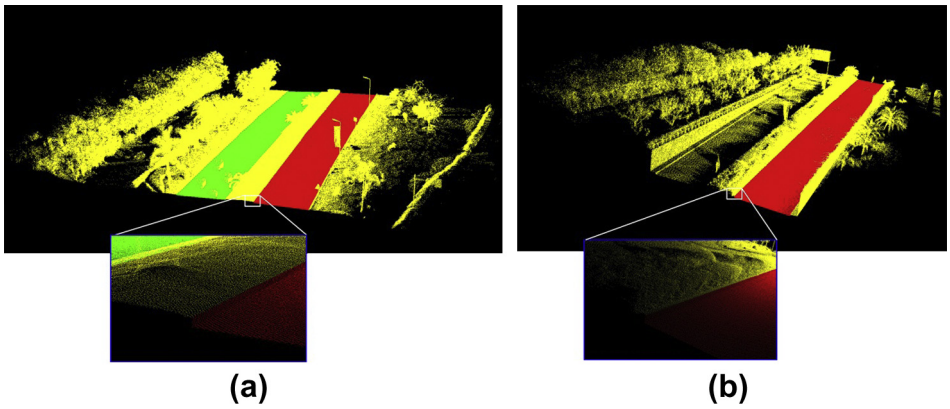

Fig. 6. The results of road extraction based on curbs: (a) Huangdao and (b) ICEC datasets.

Table 2
Parameters in the road marking extraction.

Stage	Name	Definition	Value
The generation of the geo-referenced intensity image	α	Distance weight	0.5
	β	Intensity weight	0.5
	r_g	Image resolution	To be decided
The extraction of the road markings	N_s	Number of bins	Automatically determined by the point density
	T_i	Segmentation thresholds	Automatically determined by the Otsu's method
	l	Structuring element size	To be decided
	θ	Structuring element direction	Automatically determined by the trajectory data

in this study. As a result, the ICEC and Huandao datasets are comprised of 35 and 21 blocks, respectively. Each profile is sliced from each block. Correspondingly, with a profile width S_g of 0.25 m, there are 35 profiles for the ICEC dataset, and 21 profiles for the Huandao dataset, respectively. Through experimentation, a profile is segmented into a set of grids, with each grid containing about 40 points and having a grid width *Sp* of 0.05 m. Finally the profile is converted into a pseudo scan line using the principal points estimated from the grid cells by a Quick Sort Algorithm. Prior knowledge of curbs allowed us to keep the curb height range between 0.08 m and 0.3 m.

Using these pre-defined thresholds, the curb corners are extracted from the profiles and fitted into two smooth edges of the roads using the cubic B-Spline fitting method. Fig. 6 shows the separated results of road from non-road points with our curb-based road extraction method. The close-up views in the white rectangles demonstrate that the road surfaces are accurately extracted.

4.2. Extraction of road markings

From the generation of the geo-referenced intensity image to the extraction of the road markings, there are several parameters

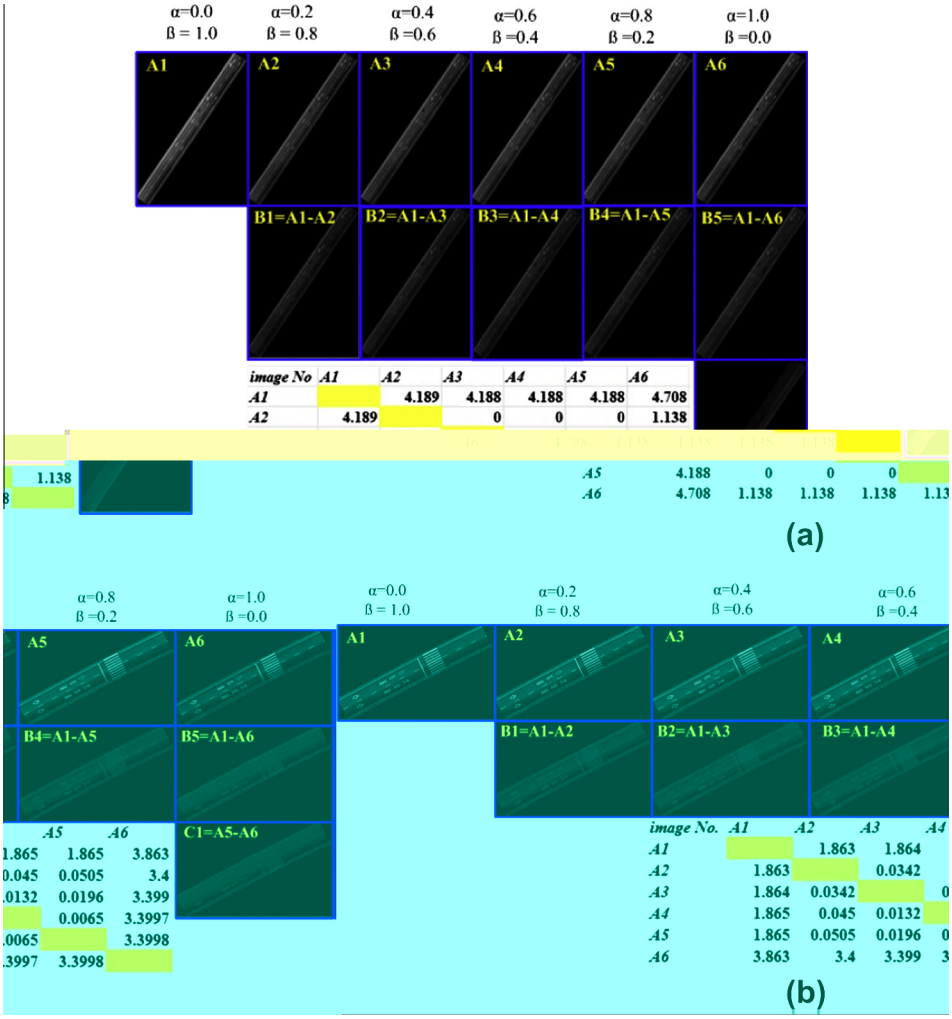

Fig. 7. Different geo-referenced intensity images under different α and β with the grid size of 0.04: (a) Huandao and (b) ICEC.

involved, as detailed in Table 2. Among these parameters, the number of bins is determined by the point density, and the segmentation thresholds (T_i) are automatically calculated by the Otsu's method; the direction (θ) of the linear structuring element depends on the trajectory data.

4.2.1. Generation of geo-referenced intensity Images

The weight coefficients α and β are used to control the contributions of both the distance and intensity to the grey value of a grid cell during implementation of the extended IDW interpolation. We tested the following different groups of weight coefficients α and β: (0.0,1.0), (0.2,0.8), (0.4,0.6), (0.6,0.4), (0.8,0.2), and (1.0,0.0), and then, as shown in Fig. 7, generated six geo-referenced intensity images, respectively, ranging from A1 to A6. For example, the comparative results of B1 (Image A1 minus Image A2) and C1 (Image A5 minus Image A6) show that both the intensity and distance information contribute to the grey values of the geo-referenced intensity image. In Fig. 8, Images A2 to A5 (see row 1) and Images B1 to B4 (see row 2) demonstrate that the quality of the geo-referenced intensity images is relatively stable when the weight coefficient α changes from 0.2 to 0.8, and the weight coefficient β from 0.8 to 0.2, accordingly. To investigate the changes among the geo-referenced intensity images, a pixel-level difference ($P_{pld} = \sum G_i / N_{change}$) was used to describe the difference between two images (Yang et al., 2013), where $\sum G_i$ denotes the sum of grey values of the changed pixels, and N_{change} is the number of the changed pixels. The pixel-level-difference tables in Fig. 7(a) and (b) confirm that there is no improvement or change among the four images (A2, A3, A4, A5) with weight coefficients α and β as (0.2,0.8), (0.4,0.6), (0.6,0.4), (0.8,0.2). As a result, in the following experiments, we apply the weight coefficients α and β of (0.5,0.5) to the road points for generating geo-referenced intensity images.

In Eq. (4), the intensity weight $W^{I}_{k,ij}$ includes the following two parts: $W^{I1}_{k,ij}$ and $W^{I2}_{k,ij}$ for the local and global information, respectively. The global weight $W^{I2}_{k,ij}$ functions as an equalizer that stretches the grey values of the geo-referenced intensity image for contrast adjustment, thus allowing for areas of lower contrasts to gain higher contrasts. Fig. 8 shows a comparison of images with and without the global weights (images *A2* and *a2*). Image *A2–a2* is the result of image *A2* minus image *a2*, indicating that the use of the global weight increases intensity contrast. The vertical profiles *B* and *B′* also confirm that the contrast between the background and foreground in image *A2* are greater than those in image *a2*. Through this global adjustment, the intensities can be better distributed for road-marking extraction.

4.2.2. Point-density-dependent multi-threshold segmentation

To test the performance of the multi-threshold segmentation, comparisons were made with fixed thresholds on the eight road-marking images selected from two datasets. Table 3 summarizes road-marking types on the eight images; each road-marking image includes two or three types of road markings. To the best of our knowledge, currently there is no dataset that is designed for

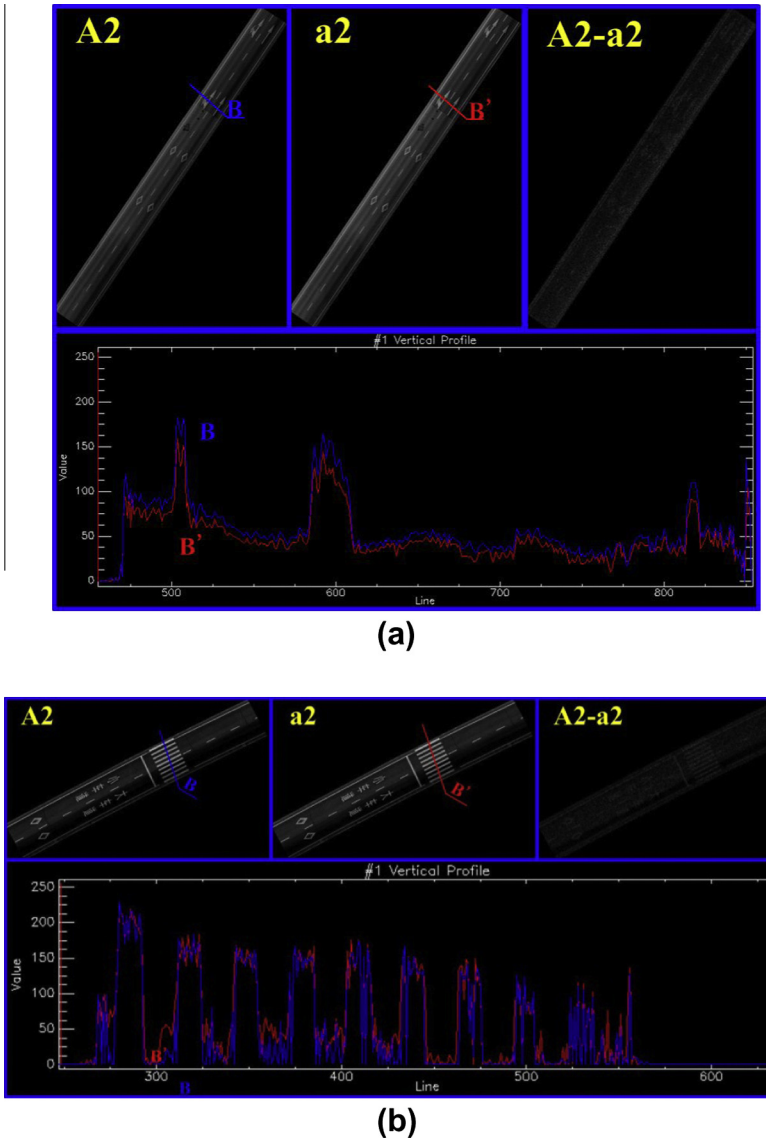

Fig. 8. Intensity equalization with and without global information: (a) Huandao and (b) ICEC.

Table 3
types of road markings in the eight road-marking images.

Image Name	Types of road markings
Marking 1	Arrow markings, solid edgeline and broken laneline markings
Marking 2	Symbol markings, solid edgeline and broken laneline markings
Marking 3	Word markings, solid edgeline and broken laneline markings
Marking 4	Solid edgeline and broken laneline markings
Marking 5	Crosswalk markings
Marking 6	Arrow markings, symbol markings, solid edgeline and laneline markings
Marking 7	Hatch markings
Marking 8	Hatch markings and solid line markings

evaluating the performance of road-marking detection and recognition from MLS systems.

We set the weight coefficients as $\alpha = 0.5$, $\beta = 0.5$, and the image resolution as $r_g = 0.04$ m for generating the geo-referenced intensity image. The eight road-marking examples are shown in Fig. 9. The second row presents the segmentation results using the optimal single thresholds achieved by the Otsu's method. This results in the emergence of noises on one side of every road. In addition, a part of the road markings are missing on the other side. For example, the Otsu's method suggests that the grey value of 60 is the optimal threshold for Marking 1 to separate the foreground (road markings) from the background. The segmentation results, however, show that the lane-marking on the top is barely identified, although the turn-left-and-straight-ahead and straight-ahead arrow-markings are almost completely detected. Therefore, it is difficult to keep a trade-off between correctness and completeness of road markings using a universal threshold.

Compared to the results in the second row, all results in the third row indicate that the proposed point-density-dependent multi-threshold segmentation method provides optimal local thresholds to identify all road markings correctly and completely, regardless of road materials and dimensions.

4.2.3. Morphological operation

To explore the impact of structuring element size on road-marking extraction, we search a range of l (3,5,7,9,11) for the eight road markings, while keeping $\alpha = 0.5$, $\beta = 0.5$, and $r_g = 0.04$ m. Fig. 10 displays the road-marking extraction results on the eight examples with five sizes of horizontal structuring elements. Visual

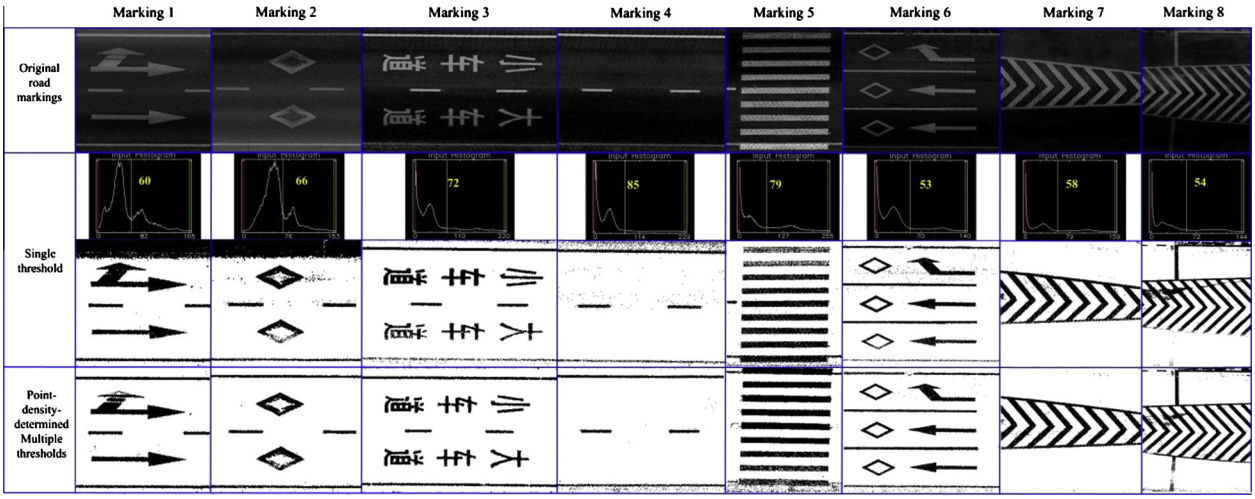

Fig. 9. A comparison of the point-density-dependent multi-threshold method and the fixed threshold.

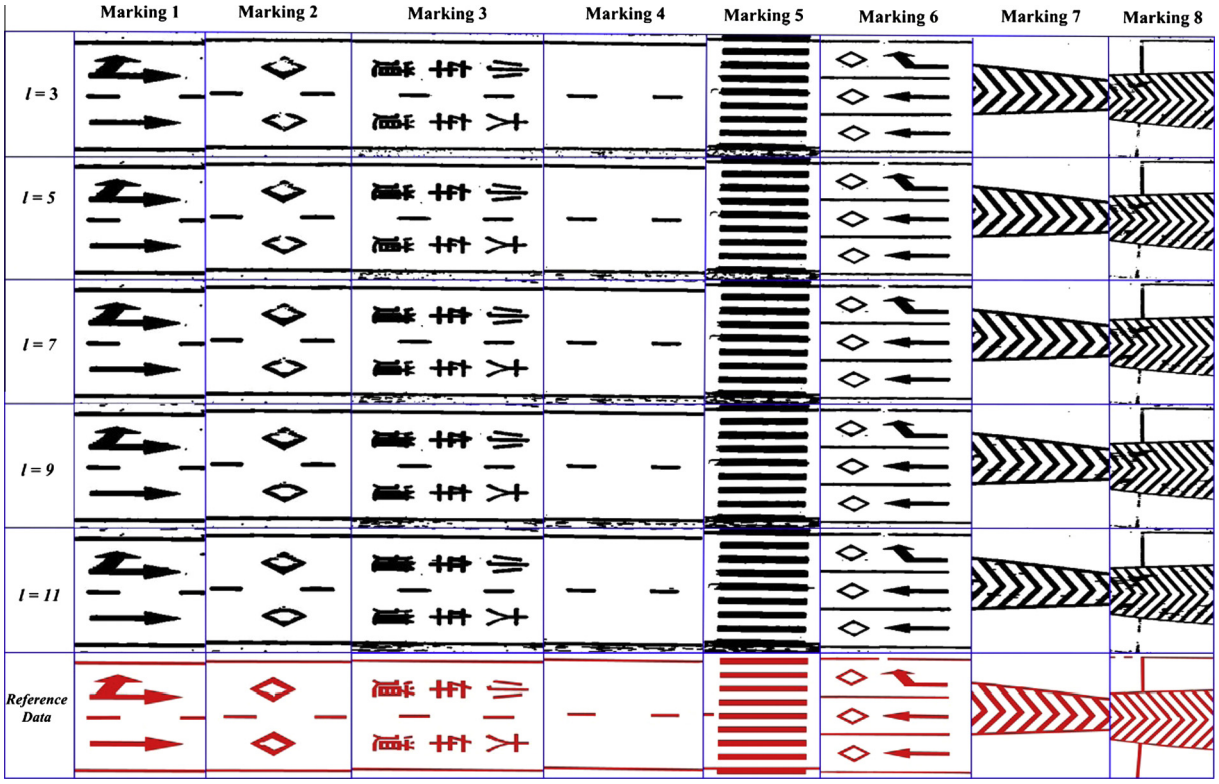

Fig. 10. Eight road markings under different sizes of a linear structuring element.

inspection suggests that there was no significant change for most road markings when l was increased from 3 to 5. However, along the road edges, small areas of noise become larger after performing the morphological closing operation. In addition, the road markings are gradually dilated with increasing kernel size. Particularly, the word markings within Marking 3 are severely dilated since l increases from 5 to 11.

By comparing the extracted road markings with the manually interpreted ground-truth, we quantitatively evaluated the results of the road markings using the following three measures: completeness (*cpt*), correctness (*crt*), and *F-measure*. *cpt* describes how complete the extracted road markings are, while *crt* indicates what percentage of the extracted road markings are valid. The *cpt* is expressed as $cpt = C_p/Rf$ and *crt* is defined as $crt = C_p/E_p$, where C_p denotes the number of pixels belonging to the actual road markings, Rf is the ground-truth collected by the manual interpretation method, and E_p represents the number of pixels extracted by the proposed algorithm. *F-measure* is an overall score, defined as $F = 2 \times \frac{(cpt \cdot crt)}{(cpt+crt)}$.

Fig. 11 shows the measures of road-marking extraction results on eight images with five different sizes of the structuring kernels. The results of all eight samples demonstrate that the completeness index *cpt* increases when the structuring-kernel size increases from 3 to 7, while the *cpt* remains stable when the structuring-kernel size is over 7. The correctness index *crt*, on the contrary, decreases with the increasing size of the structuring kernel.

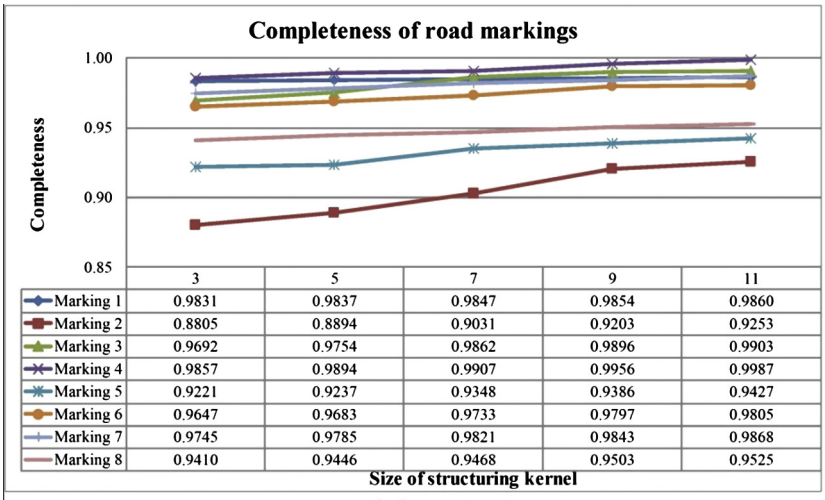

	3	5	7	9	11
Marking 1	0.9831	0.9837	0.9847	0.9854	0.9860
Marking 2	0.8805	0.8894	0.9031	0.9203	0.9253
Marking 3	0.9692	0.9754	0.9862	0.9896	0.9903
Marking 4	0.9857	0.9894	0.9907	0.9956	0.9987
Marking 5	0.9221	0.9237	0.9348	0.9386	0.9427
Marking 6	0.9647	0.9683	0.9733	0.9797	0.9805
Marking 7	0.9745	0.9785	0.9821	0.9843	0.9868
Marking 8	0.9410	0.9446	0.9468	0.9503	0.9525

Size of structuring kernel

(a)

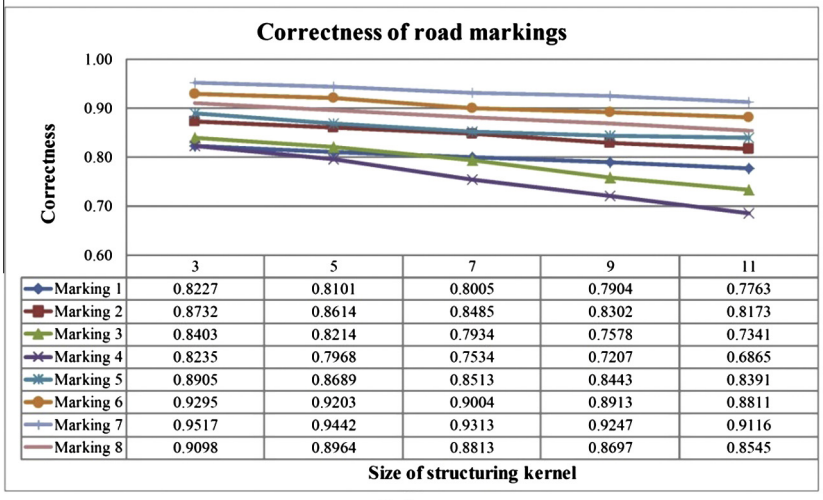

	3	5	7	9	11
Marking 1	0.8227	0.8101	0.8005	0.7904	0.7763
Marking 2	0.8732	0.8614	0.8485	0.8302	0.8173
Marking 3	0.8403	0.8214	0.7934	0.7578	0.7341
Marking 4	0.8235	0.7968	0.7534	0.7207	0.6865
Marking 5	0.8905	0.8689	0.8513	0.8443	0.8391
Marking 6	0.9295	0.9203	0.9004	0.8913	0.8811
Marking 7	0.9517	0.9442	0.9313	0.9247	0.9116
Marking 8	0.9098	0.8964	0.8813	0.8697	0.8545

Size of structuring kernel

(b)

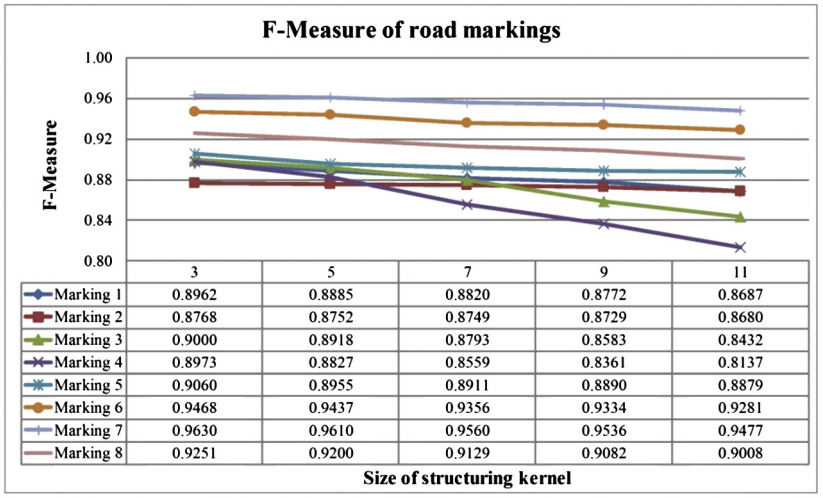

	3	5	7	9	11
Marking 1	0.8962	0.8885	0.8820	0.8772	0.8687
Marking 2	0.8768	0.8752	0.8749	0.8729	0.8680
Marking 3	0.9000	0.8918	0.8793	0.8583	0.8432
Marking 4	0.8973	0.8827	0.8559	0.8361	0.8137
Marking 5	0.9060	0.8955	0.8911	0.8890	0.8879
Marking 6	0.9468	0.9437	0.9356	0.9334	0.9281
Marking 7	0.9630	0.9610	0.9560	0.9536	0.9477
Marking 8	0.9251	0.9200	0.9129	0.9082	0.9008

Size of structuring kernel

(c)

Fig. 11. Eight road markings with different structuring element sizes, ranging from 3 to 11, (a) completeness, (b) correctness and (c) F measure.

Particularly, the *crt* index of Marking 4 quickly declines, followed by Marking 3 (the word marking). The dilation operation causes this downward trend. As the structuring kernel increases in size, the dilation operation not only fills the holes in the road markings, but also merges small areas of noise into large areas of noise, and merges noise into the road markings. In our study, with an image

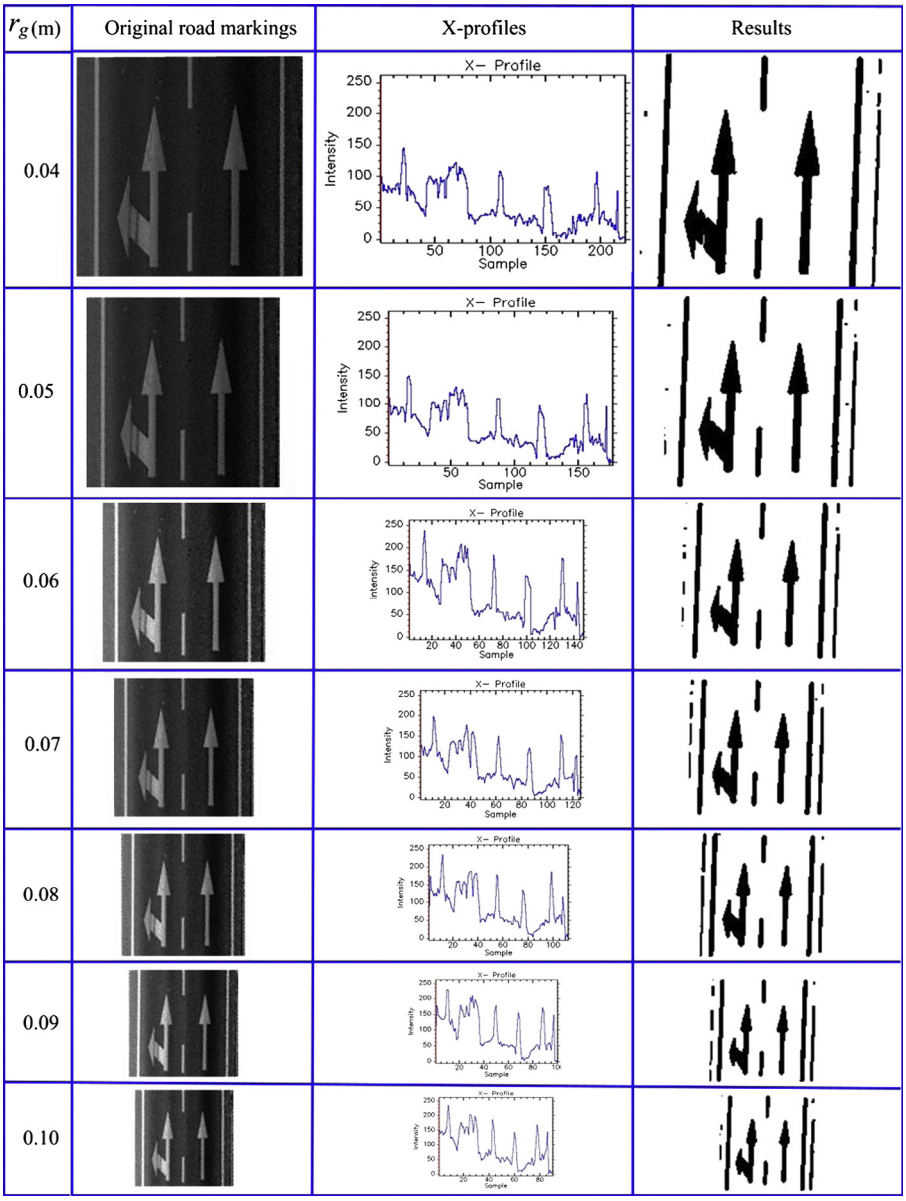

Fig. 12. The road marking with different image resolution: (a) qualitative assessment and (b) quantitative assessment.

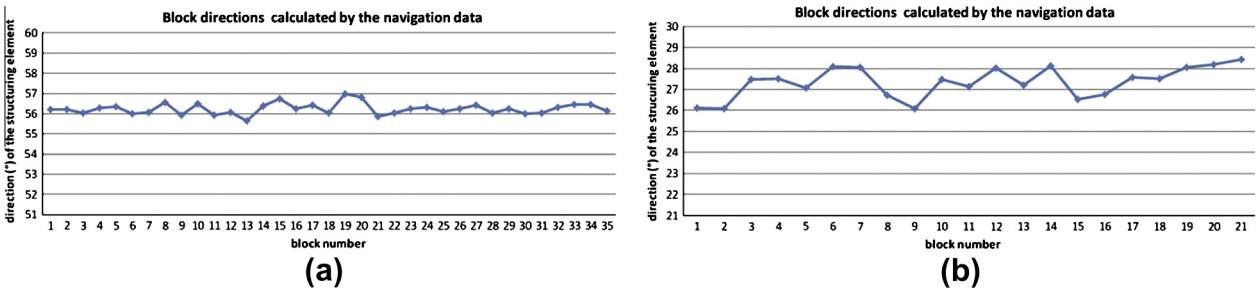

Fig. 13. directions of the linear structuring element: (a) Huandao and (b) ICEC.

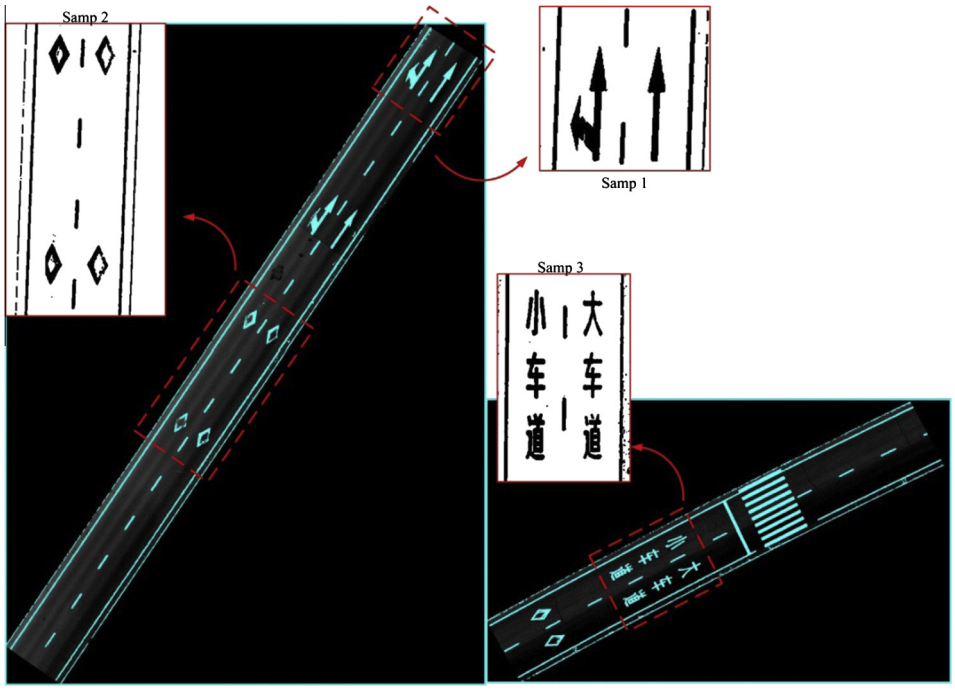

Fig. 14. The final results of road markings overlaid on the geo-referenced intensity images: (a) Huandao and (b) ICEC datasets.

Table 4
Road-marking performance.

	Sample	*cpt*	*crt*	*F-measure*
Huandao	Samp 1	0.98	0.82	0.89
	Samp 2	0.91	0.86	0.88
	All	0.94	0.83	0.88
ICEC	Samp 3	0.98	0.84	0.90
	All	0.97	0.82	0.90
Average		0.96	0.83	0.89

resolution of r_g = 0.04 m, the best size of the structuring kernel was obtained at l = 3.

4.2.4. Impact of image resolution on our algorithm

Since road markings, under different image resolutions, can be presented with different details, the image resolution is one of the very critical parameters for extracting road markings. To evaluate the sensitivity of the image resolution relative to the performance of our road-marking extraction algorithm, we tested one block data with a range of r_g (0.04 m, 0.05 m, 0.06 m, 0.07 m, 0.08 m, 0.09 m, and 0.10 m) while keeping α = 0.5, β = 0.5.

Fig. 12(a) shows the extracted road-markings on seven images with different image resolutions. The first column shows that details of the arrow-and-lane marking are inversely proportional to the image resolutions. The second column displays the X-profile data of the arrow-and-lane markings. The horizontal axis represents the widths of the arrow-and-lane-marking image; the vertical axis represents the intensity values of pixels along the X-profiles. Note that the intensity values vary from one image to the other with the image resolution. The extracted road markings are shown in the third column. Visual inspection suggests that the shapes of the arrow-and-lane markings are preserved almost completely for seven test cases.

To assess our road-marking algorithm, a comparative analysis was completed. The calculated *crt*, *cpt* and *F-measure* indices are shown in Fig. 12(b). For all the cases, the *crt* values are greater than 0.74, the *cpt* values are higher than 0.94, and the *F-measure* values range from 0.84 to 0.9. Note that there are slight changes in these three measure indices when the image resolution increases from 0.04 m to 0.05 m. However, the *crt*, *cpt* and *F-measure* values slowly decrease when the image resolution is greater than 0.05 m. Thus, we selected the image resolution of either 0.04 m or 0.05 m as the most applicable values to generate the geo-referenced intensity images from the RIEGL MLS data.

4.2.5. Overall performance

Two tests were conducted on the Huandao and ICEC datasets to assess the overall performance of our algorithm. According to the sensitivity analysis, we kept R_g = 3.0 m, S_p = 0.05 m, S_g = 0.2 m, G_{min} = 0.08 m, and G_{max} = 0.3 m for the curb-based road extraction. Since there are no sharp turns or curves of the roads in two cases, we kept R_g = 3.0 m. With R_g = 3.0 m, the Huandao and ICEC datasets have 35 and 21 blocks and profiles, respectively. Afterwards, we kept α = 0.5, β = 0.5, and r_g = 0.04 to generate geo-referenced intensity images from the extracted road points.

In each block, we employed the point-density-dependent segmentation method to automatically obtain multiple thresholds for segmenting possible road markings. For all blocks, the size of the structuring element l was 3, while θ was calculated by the trajectory data. To simplify the task, we provided a fixed value for each block via the trajectory data. Fig. 13 shows the values of θ for 35 blocks and 21 blocks of Huandao and ICEC datasets, respectively. After segmenting with multiple thresholds, the morphological closing operation was used to fill up the holes and remove the noise in the segmented road markings. Fig. 14 shows the extracted road markings overlaid on the geo-referenced intensity image. To evaluate our road-marking extraction algorithm, three samples were selected from two datasets as follows: samples 1 and 2 from the Huandao dataset, and sample 3 from the ICEC dataset. The close-up views show that our method produces complete road markings with less noise. The statistical results listed in Table 4 display that the average *cpt*, *crt*, and *F-measure* values are 0.96, 0.83, and 0.89, respectively. In addition, the values of the three measures are quite stable for all samples, indicating that our road-marking method is robust to different types of road markings.

4.3. Computational complexity

Through the use of a 3.30 GHz Intel(R) Core(TM) i3-2120 CPU, the running time of the proposed method for processing the 8.4-million-point Huandao and 5.4-million-point ICEC datasets are about 1.11 and 0.89 s, respectively. The total running time does not include the data preparation time, which is the time of sectioning the raw data into a number of blocks and profiles. The reason is that the processing time of the data preparation is highly dependent on the reading-and-writing speed of the hard disk due to frequent data-interaction operations. In our algorithm, all road marking extracting operations are performed on the geo-referenced intensity images, indicating that no data indexing structures need to be built for data querying and searching. Furthermore, the computation and processing time can be reduced if the stand-alone operation is replaced by a distributed processing system under a virtualization environment. Therefore, the integration of the proposed road-marking processing algorithm and the affordable hardware is a promising solution to computational efficiency of MLS data.

5. Conclusion

This paper proposed a road-marking extraction algorithm using MLS data, which consists of (1) the curb-based extraction of road surfaces, (2) the generation of geo-referenced intensity images with a histogram equalization-like strategy, and (3) the extraction of road markings using the point-density-dependent multi-threshold segmentation and morphological closing operation.

The two datasets collected by the RIEGL VMX-450 MLS system were used in this paper to validate our road-marking extraction method. The two test datasets cover a total of around 168 m of roadway that contain several types of road markings. The experimental results demonstrated that our method is able to extract road markings with a completeness of 0.96, a correctness of 0.83, and an *F-measure* of 0.89. Our method for extracting road markings in large volumes of MLS datasets is effective since (1) no data indexing structures are built for searching and querying, (2) the extracted road surface serves prior knowledge that facilitates the road-marking processing and improves the correctness of road markings, (3) a combination of local and global intensity weights contributes to the generation of a 2D geo-referenced intensity image, and (4) dynamic thresholds determined by point density overcomes inconsistent intensity values caused by incidence angle of laser pulses and range of the scanner center to the illuminated road surface.

Acknowledgement

The authors would like to acknowledge Mr. Michael McAllister, sessional lecturer at the School of Information Science and Engineering, Xiamen University, China for proofreading the manuscript. The authors would also like to acknowledge the anonymous reviewers for their valuable comments.

References

Carnaby, B., 2005. Poor road markings contribute to crash rates. In: Australasian Road Safety Research Policing Education Conference, Wellington, New Zealand, 14–16 November, CD-ROM (CD401).

Charbonnier, P., Diebolt, F., Guillard Y., Peyret, F., 1997. Road markings recognition using image processing. In: IEEE Conference on Intelligent Transportation System, Boston, MA, USA. 12–12 November, pp. 912–917.

Chehata, N., Guo, L., Mallet, C., 2009. Airborne lidar feature selection for urban classification using random forest. In: The International Archives of the Photogrammetry, Remote Sensing and Spatial Information Sciences 39 (3/W8), pp. 207–212.

Chen, X., Stroila, M., Wang, R., 2009. Next generation map marking: geo-referenced ground-level LiDAR point clouds for automatic retro-reflective road feature extraction. In: 17th ACM SIGSPATIAL International Conference on Advances in Geographic Information System, Seattle, WA, 4–6 November (on CD-ROM).

Danescu, R., Nedevschi, S., 2010. Detection and classification of painted road objects for intersection assistance applications. In: Proc. of IEEE Conference on Intelligent Transportation System, Funchal, Portugal, 19–22 September, pp. 433–438.

Gordon, P., 2010. An Introduction to the Technology Mobile Mapping Systems, http://web2.ges.gla.ac.uk/~gpetrie/Petrie_Mobile_Mapping_Systems_Jan-Feb_2010.pdf, (accessed 04.11.13).

Graham, L., 2010. Mobile mapping system overview. Photogrammetric Engineering & Remote Sensing 76 (3), 222–229.

Haala, N., Peter, M., Cefalu, A., Kremer, J., 2008. Mobile lidar mapping for urban data capture, In: Proceedings of the 14th International Conference on Virtual Systems and Multimedia, Limassol, Cyprus. 20–25 October 2008, pp. 101–106.

Jaakkola, A., Hyyppä, J., Hyyppä, H., Kukko, A., 2008. Retrieval algorithms for road surface modelling using laser-based mobile mapping. Sensors 8, 5238–5249.

Kheyrollahi, A., Breckon, T.P., 2010. Automatic real-time road marking recognition using a feature approach. Machine Vision and Applications 23 (1), 123–133.

Li, Y., He, K., Jia, P., 2007. Road markers recognition based on shape information. In: IEEE International Symposium on Intelligent Vehicles Symposium, Istanbul, Turkey, 13–15 June, pp. 117–122.

Li, W., Lu, G., Wang, Y., 1997. Recognizing white line markings for vision-guided vehicle navigation by fuzzy reasoning. Pattern Recognition Letters 18, 771–780.

McCall, J.C., Trivedi, M.M., 2006. Video based lane estimation and tracking for driver assistance: survey, system, and evaluation. IEEE Transactions on Intelligent Transportation Systems 7 (1), 20–37.

McCarthy, T., Fotheringham, A.S., Charlton, M., Winstanley, A., O'Malley, V., 2007. Integration of LiDAR and stereoscopic imagery for route corridor surveying. In: Mobile Mapping Technology 2007, Padua, Italy, 28–31 May, 37, pp. 1125–1130.

Otsu, N., 1979. A threshold selection method from grey-level histograms. IEEE Transactions on Systems, Man, and Cybernetics SMC-9 (1), 62–66.

Rebut, J., Bensrhair, A., Toulminet, G., 2004. Image segmentation and pattern recognition for road marking analysis. IEEE International Symposium Industrial Electronics 1 (4–7), 727–732.

RIEGL, 2013. RIEGL VQ-450, http://www.riegl.com/nc/products/mobile-scanning/produktdetail/product/scanner/31/, (accessed 04.11.13).

Smadja, L., Ninot, J., Gavrilovic, T., 2010. Road extraction and environment interpretation from lidar sensors. The International Archives of the Photogrammetry, Remote Sensing and Spatial Information Sciences 38 (3A), 281–286.

Toth, C., Paska, E., Brzezinska, D., 2008. Using road pavement markings as good control for lidar data. The International Archives of the Photogrammetry, Remote Sensing and Spatial Information Sciences 37 (B1), 189–196.

Ussyshkin, V., 2009. Mobile laser scanning technology for surveying application: from data collection to end-products, FIG Working Week 2009, Eilat, Israel, 3–8 May (on CD-ROM).

Vosselman, G., 2009. Advanced point cloud processing. Photogrammetric Week'09, Heidelberg, Germany, pp. 137–146.

Wang, N., Liu, W., Zhang, C., Yuan, H., Liu, J., 2009. The detection and recognition of arrow markings recognition based on monocular vision. In: Chinese Control and Decision Conference, Guilin, China, 17–19 June, pp. 4380–4386.

Yang, B., Fang, L., Li, Q., Li, J., 2012. Automated extraction of road markings from mobile lidar point clouds. Photogrammetric Engineering & Remote Sensing 78 (4), 331–338.

Yang, B., Fang, L., Li, J., 2013. Semi-automated extraction and delineation of 3d roads of street scene from mobile laser scanning point clouds. ISPRS Journal of Photogrammetry and Remote Sensing 79, 80–93.